

# Preliminary numerical study on long-wavelength wave propagation in a jointed rock mass

Song-Hun Chong<sup>1a</sup>, Ji-Won Kim<sup>2b</sup>, Gye-Chun Cho<sup>\*2</sup> and Ki-Il Song<sup>3c</sup>

<sup>1</sup>Department of Civil Engineering, Sunchon National University 255 Jungang-ro, Sunchon, Jeollanam-do 57922, Republic of Korea

<sup>2</sup>Department of Civil and Environmental Engineering, KAIST, 291 Daehak-ro, Yuseong-gu, Daejeon 34141, Republic of Korea

<sup>3</sup>Department of Civil Engineering, Inha University, 100 Inha-ro, Michuhol-gu, Incheon 22212, Republic of Korea

(Received January 17, 2020, Revised March 12, 2020, Accepted March 17, 2020)

**Abstract.** Non-destructive exploration using elastic waves has been widely used to characterize rock mass properties. Wave propagation in jointed rock masses is significantly governed by the characteristics and orientation of discontinuities. The relationship between spatial heterogeneity (i.e., joint spacing) and wavelength for elastic waves propagating through jointed rock masses have been investigated previously. Discontinuous rock masses can be considered as an equivalent continuum material when the wavelength of the propagating elastic wave exceeds the spatial heterogeneity. However, it is unclear how stress-dependent long-wavelength elastic waves propagate through a repetitive rock-joint system with multiple joints. A preliminary numerical simulation was performed in this study to investigate long-wavelength elastic wave propagation in regularly jointed rock masses using the three-dimensional distinct element code program. First, experimental studies using the quasi-static resonant column (QSRC) testing device are performed on regularly jointed disc column specimens for three different materials (acetal, aluminum, and gneiss). The P- and S-wave velocities of the specimens are obtained under various normal stress levels. The normal and shear joint stiffness are calculated from the experimental results using an equivalent continuum model and used as input parameters for numerical analysis. The spatial and temporal sizes are carefully selected to guarantee a stable numerical simulation. Based on the calibrated jointed rock model, the numerical and experimental results are compared.

**Keywords:** rock mass; elastic wave velocity; quasi-static resonant column test; joint stiffness; DEM simulation

## 1. Introduction

Elastic-wave-based exploration techniques are widely used in geotechnical and rock engineering, from infrastructure construction (e.g., rock slopes and tunnels) to resource recovery and production (e.g., geothermal development and petroleum production). Data interpretation for wave propagation in jointed rock masses requires a comprehensive understanding of joint characteristics, such as joint spacing, joint roughness, and joint stiffness, as well as incident wave characteristics, such as amplitude and wavelength (Pyrak-Nolte *et al.* 1990, Ju *et al.* 2007, Zhao *et al.* 2008). Wave propagation in jointed rock masses is often modeled using the displacement discontinuity model (DDM), where stresses across joint interfaces are continuous, whereas particle displacements are not during stress wave propagation (Mindlin 1960, Schoenberg 1980). Various theoretical and numerical investigations based on

the DDM have been performed for wave propagations through multiple parallel fractures (Cai and Zhao 2000, Zhao *et al.* 2008, Perino *et al.* 2010, Zhu *et al.* 2013), non-parallel joints (Chai *et al.* 2016), filled joints (Zhu *et al.* 2012, Li *et al.* 2013, Wang *et al.* 2017), and obliquely incident waves (Li *et al.* 2014, Li *et al.* 2016) using various analytical models.

Meanwhile, the equivalent medium model (EMM) corresponding to the long-wavelength propagation can be used to formulate an effective modulus representing the effects of joints on rock mass properties (Schoenberg and Muir 1989, Cook 1992, Li *et al.* 2010). Although the EMM oversimplifies the jointed rock mass properties and is not applicable when fractures are relatively large and sparsely spaced, it can be used to interpret wave propagation characteristics under the long-wavelength assumption, where the wavelength is much longer than the spatial heterogeneity (i.e., joint spacing). In fact, long-wavelength propagation is the most typical situation in seismology and exploration geophysics (White 1983, Schoenberg and Muir 1989, Schoenberg and Sayers 1995).

Several laboratory scale studies have been conducted to understand long-wavelength propagation in jointed rock masses more effectively. Fratta and Santamarina (2002) invented the quasi-static resonant column (QSRC) testing device based on the long-wavelength S-wave propagation of a jointed rock mass under various normal stress levels and investigated the effects of joint thickness filled with clay gouge. Cha *et al.* (2009) performed experimental tests

\*Corresponding author, Professor

E-mail: [gyechun@kaist.ac.kr](mailto:gyechun@kaist.ac.kr)

<sup>a</sup>Assistant Professor

E-mail: [shchong@snu.ac.kr](mailto:shchong@snu.ac.kr)

<sup>b</sup>Ph.D. Candidate

E-mail: [g1kim@kaist.ac.kr](mailto:g1kim@kaist.ac.kr)

<sup>c</sup>Associate Professor

E-mail: [ksong@inha.ac.kr](mailto:ksong@inha.ac.kr)

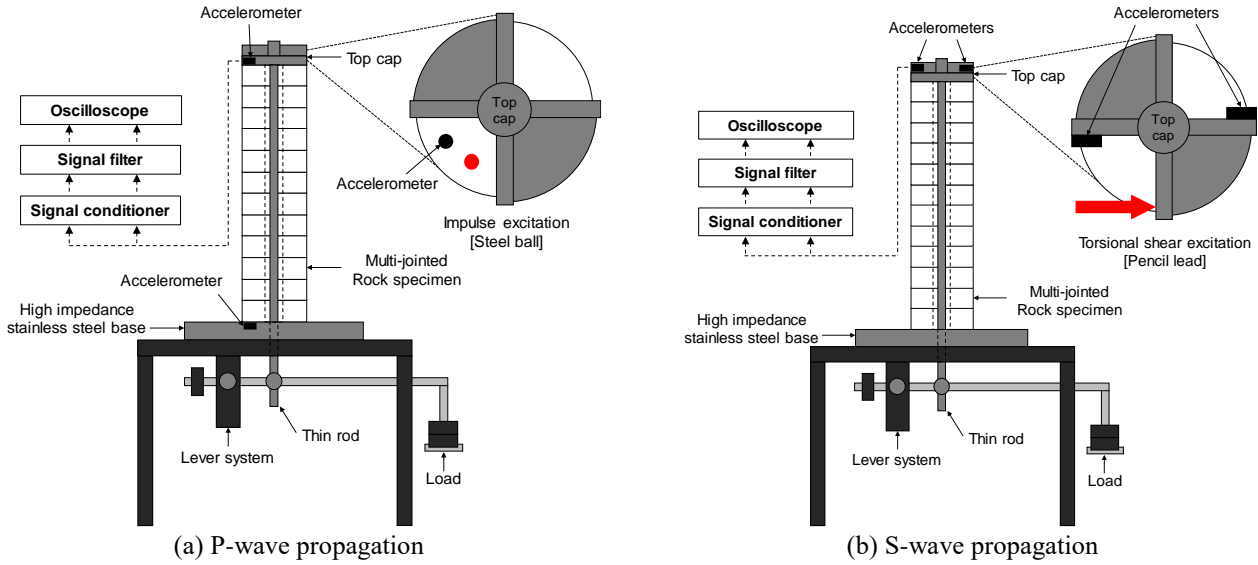


Fig. 1 Quasi-static resonant column(QSRC) test setup to measure long-wavelength wave propagation in jointed rock

on long-wavelength P- and S-wave propagations and studied S-wave attenuation characteristics in jointed rock masses subjected to various normal stress and joint conditions; they suggested an analytical model (i.e., an equivalent elastic wave velocity model) to extract joint properties from measured QSRC test data. Mohd-Nordin *et al.* (2014) investigated torsional shear wave propagation through natural rock joint surfaces and the correlation between the joint roughness coefficient and torsional shear wave velocity. Kim *et al.* (2018) conducted QSRC tests and resonant column tests on grouted rock joints and examined the effects of initial joint roughness and grout fill thickness. Previous studies regarding long-wavelength wave propagation in jointed rock masses using QSRC test devices focused on different joint conditions and lacked a numerical background on which further parametric studies could be performed.

Long-wavelength elastic wave propagations in regularly jointed rock masses are investigated herein based on the three-dimensional distinct element code (3DEC) program. Experimental studies using the QSRC test device were conducted to characterize the P- and S-wave velocities under various normal stress levels. The normal and shear joint stiffnesses were extracted from the experimental results using the equivalent continuum model and used as input parameters for numerical analysis. Using the calibrated jointed rock model, numerical results were compared with the experimental results. Further analysis can provide a better understanding on the propagation of elastic waves through the repetitive rock-joint system.

## 2. Experimental study

### 2.1 Equivalent continuum model for joint stiffness characterization

The equivalent continuum model and accompanying equivalent modulus for jointed rocks under static conditions

was suggested by Goodman (1989). The elastic constants for an equivalent continuous material representative of a rock mass with a single set of equally distant joints were derived based on the following assumptions: The rock is isotropic, homogeneous, and linearly elastic with intact rock shear modulus  $G_{intact}$ . The shear joint stiffness  $k_s$  is defined as the slope of the shear stress to the shear-strain curve until a slip occurs between the joints. When a shear stress  $\tau$  is applied, each rock block undergoes a displacement of  $(\tau/G_{intact})S$ , and each joint slips a distance of  $\tau/k_s$ . The global shear deformation can be formulated with the summation of rock and joint displacements based on displacement discontinuity. Furthermore, the interfacing joints presents a Hertzian-type contact response at the continuous shear stress. This enables the power function of stress to be used in the joint stiffness parameter. Hence, the S-wave velocity in a jointed rock mass can be expressed as follows (Brady and Brown 1993):

$$V_{S_{rm}} = \sqrt{\frac{1}{\rho_{rm}} \left[ \frac{1}{G_{intact}} + \frac{1}{S\alpha_s \left( \frac{\sigma_v}{1kPa} \right)^{\beta_s}} \right]^{-1}} \quad (1)$$

where  $\rho_{rm}$  ( $\text{kg/m}^3$ ) is the density of the rock mass;  $G_{intact}$  (kPa) is the shear modulus of the intact rock;  $S$  (m) is the joint spacing. The factor  $\alpha_s$  (kPa/m) is the baseline joint stiffness when  $\sigma_v = 1$  kPa, and the exponent  $\beta_s$  captures the stress sensitivity. The stress sensitivity and stress gradients strongly affect jointed rock mass behaviors and wave propagations (Tao *et al.* 2016, Wu *et al.* 2019). It is noteworthy that a similar derivation can be performed for the P-wave velocity using the Young modulus of intact rock  $E_{intact}$  and the corresponding normal joint stiffness parameters.

### 2.2 Experimental setup

The QSRC test setup proposed by Fratta and

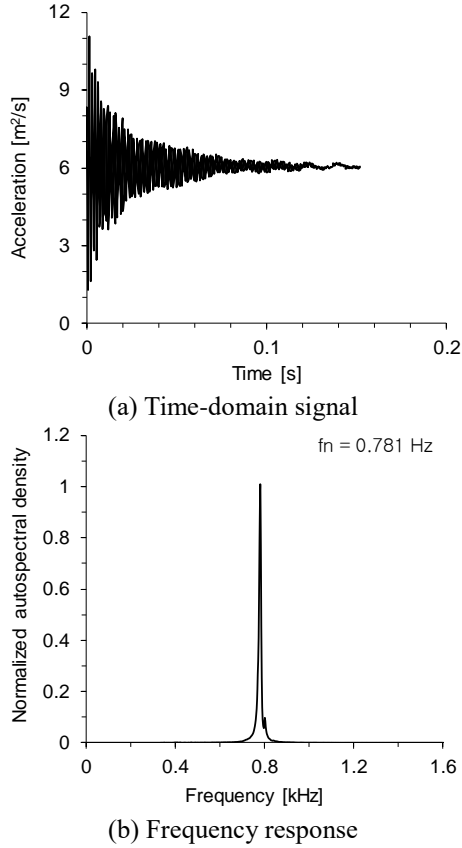


Fig. 2 Data analysis of long-wavelength S-wave velocity for gneiss specimen subjected to 297 kPa normal stress. Time domain signals are obtained from two accelerometers located on the diametrically opposite direction. Two signals were added to enhance the torsional mode

Santamarina (2002) and outlined in Cha *et al.* (2009) was reproduced to measure the long-wavelength elastic wave propagation through regularly-jointed rock mass specimens. This test setup uses quasistatic deformations below the elastic threshold level (e.g., shear strain  $< 10^{-5}$ ) to generate longitudinal and torsional excitations in jointed rock masses and measure long-wavelength P- and S-wave propagations. The QSRC testing device and electrical peripherals are shown in Fig. 1.

Jointed rock specimens with regularly spaced joints were simulated by stacking cylindrical rock discs of equal thickness. The disc surface was remained clean and flat without any undulation and filling materials. A total of 12 discs were stacked in the vertical direction for each specimen to minimize Brillouin dispersions and generate long-wavelength elastic waves (Fratta and Santamarina 2002). The specimens were placed on a high impedance steel base to simulate fixed boundary conditions at the bottom of the specimen. A light aluminum cap was placed on top of the rock column, and vertical loading was applied using a thin rod placed along the center of the discs. The upper end of the rod was anchored to the top cap to simulate a free boundary condition, and the lower end of the rod was connected to the arm of the loading frame. For all measured accelerometer signals, a signal conditioner (PCB 482A16)

Table 1 Properties of specimens used in this study

Material	Aluminum	Gneiss	Acetal
Disc thickness [mm]	250		
Diameter [mm]	63		
Density [kg/m <sup>3</sup> ]	2,780	2,704	1,410
P-wave velocity [m/s]*	6,370	4,750	1,815
Rod wave velocity [m/s]*	5,234	4,658	1,500
S-wave velocity [m/s]**	3,209	3,100	970
Poisson's ratio***	0.33	0.13	0.33
Bulk modulus [GPa]	74.6	26.4	3.2
Shear modulus [GPa]	28.6	26.0	1.2
Photograph (disc)			

\* Intact P-wave and rod wave velocities obtained from FFRC tests and point-source travel-time method

\*\* Intact S-wave velocities calculated from the following theoretical relationship (see Cha and Cho 2007):

$$V = \frac{V_P^2 - 2V_S^2}{2(V_P^2 - V_S^2)} \quad (2)$$

\*\*\* Poisson's ratio indirectly calculated from the rod wave velocity and P-wave velocity using the following equation:

$$\frac{V_{rod}^2}{V_P^2} = \frac{(1+\nu)(1-2\nu)}{(1-\nu)} \quad (3)$$

was used to amplify the measured signal, and the amplified signals were digitized using a digital storage oscilloscope (Agilent DSO6104A) and stored for post-processing.

For longitudinal excitation, a steel ball of diameter 10.3 mm was used as an impact source for stress wave generation along the longitudinal direction, as shown in Fig. 1(a). The steel ball was dropped from a height of 0.2 m onto the surface of the disc at the top of the column. The presence of the rod and weights affected the longitudinal resonance, and the column could not be considered as a free-fixed system in longitudinal vibrations. Hence, the P-wave velocity in the column system  $V_P^{QSRC}$  was calculated as the height of stacked column  $L$  divided by the travel time  $\Delta t$ , i.e.,  $V_P^{QSRC} = L/\Delta t$ . Two accelerometers placed on the top and bottom of the specimen were used to measure the travel time difference (Note: P-wave propagation is dispersive in the columns owing to the addition of radial inertia; hence, it is difficult to obtain a longitudinal resonance in a free-fixed system).

For torsional excitation, a brittle 0.5 mm mechanical pencil lead was used to excite the column at the top cap, as shown in Fig. 1(b). The fracturing of the pencil lead released the column from its initial shear deformation and enabled the specimen to vibrate freely. Two accelerometers placed on the top cap at diametrically opposite positions with their axes aligned normal to the radius of the column were used to obtain the time-domain data. Time-domain

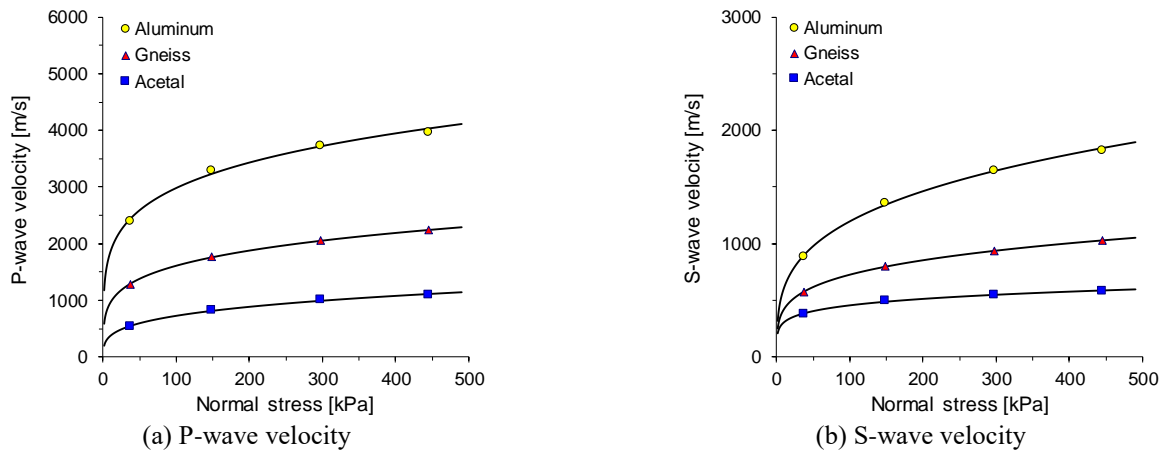


Fig. 3 Experimental results of QSRC test with different normal stress levels

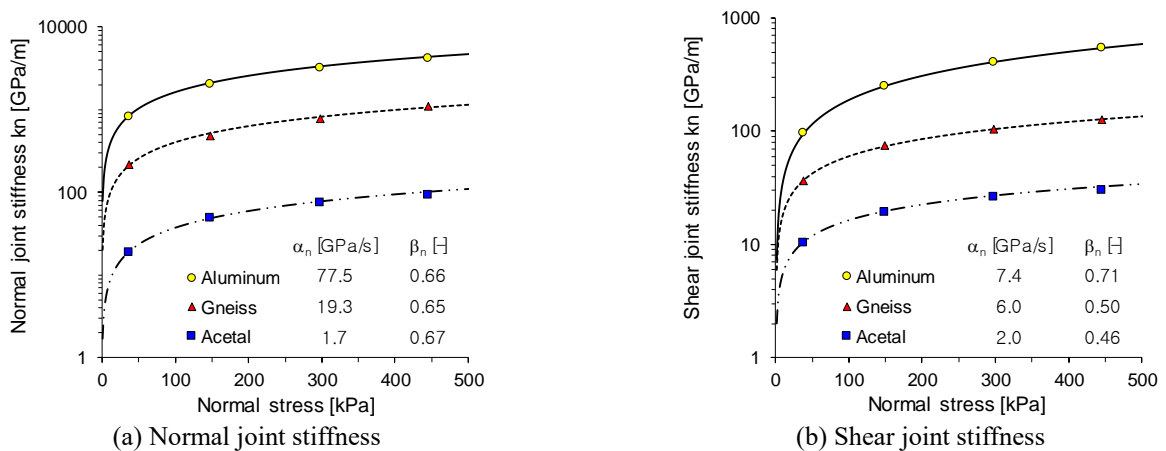


Fig. 4 Evolution of equivalent joint stiffness with different normal stress levels. The lines superimposed on data points show the fitted equation. The corresponding joint parameters are tabulated in the figures

signals were added to remove the low-frequency components of the flexural response, shown in Fig. 2(a). The added time-domain signal was then transformed to the frequency domain using fast Fourier transformation to obtain the resonance spectrum of the torsional shear response. For the given boundary conditions of the free-fixed system, the wavelength  $\lambda$  is four times the height of the stacked disc column  $L$ . Hence, the resonant frequency  $f_n$  of the torsional shear response shown in Fig. 2(b) was used to compute the long-wavelength S-wave velocity.

Three different types of specimens were tested in this study: aluminum, acetal, and gneiss. The properties of the specimens used in this study are summarized in Table 1. The rod wave and P-wave velocities of the intact block were obtained from free-free resonant column (FFRC) tests using the point-source travel-time method, and the S-wave velocities were calculated from the theoretical relationship outlined in Cha and Cho (2007). The material properties were used to calculate the normal and shear joint stiffness and assigned to the material properties (i.e., density, Poisson's ratio, shear modulus, and bulk modulus) of the disc specimens for numerical simulation. Experimental tests were conducted for four different normal stress levels (37, 148, 297, and 445 kPa) to examine the relation between the wave velocities and normal stress.

## 2.3 Experimental results

Fig. 3 shows the long-wavelength P- and S-wave velocities of the three tested materials for different normal stress levels. The velocities increased with the normal stress, which is consistent with results from previous studies (Fratta and Santamarina 2002, Cha *et al.* 2009). The normal and shear joint stiffness of each test specimen are presented in Fig. 4 according to the level of normal stress. The joint stiffness parameters  $\alpha_n$  and  $\beta_n$  for the P-wave velocity and  $\alpha_s$  and  $\beta_s$  for the S-wave velocity were estimated by best fitting the experimental data using the least-squares method, as tabulated in Fig. 4. As the normal stress increased, the normal and shear joint stiffness increased as well. The stress-dependent normal and shear joint stiffness values are representative of the stiffness characteristics of the jointed specimen at the given normal stress level and can be used in numerical analysis and as input parameters for joint interfaces.

## 3. Numerical study

### 3.1 Geometry and boundary conditions

Numerical studies were performed using the 3DEC

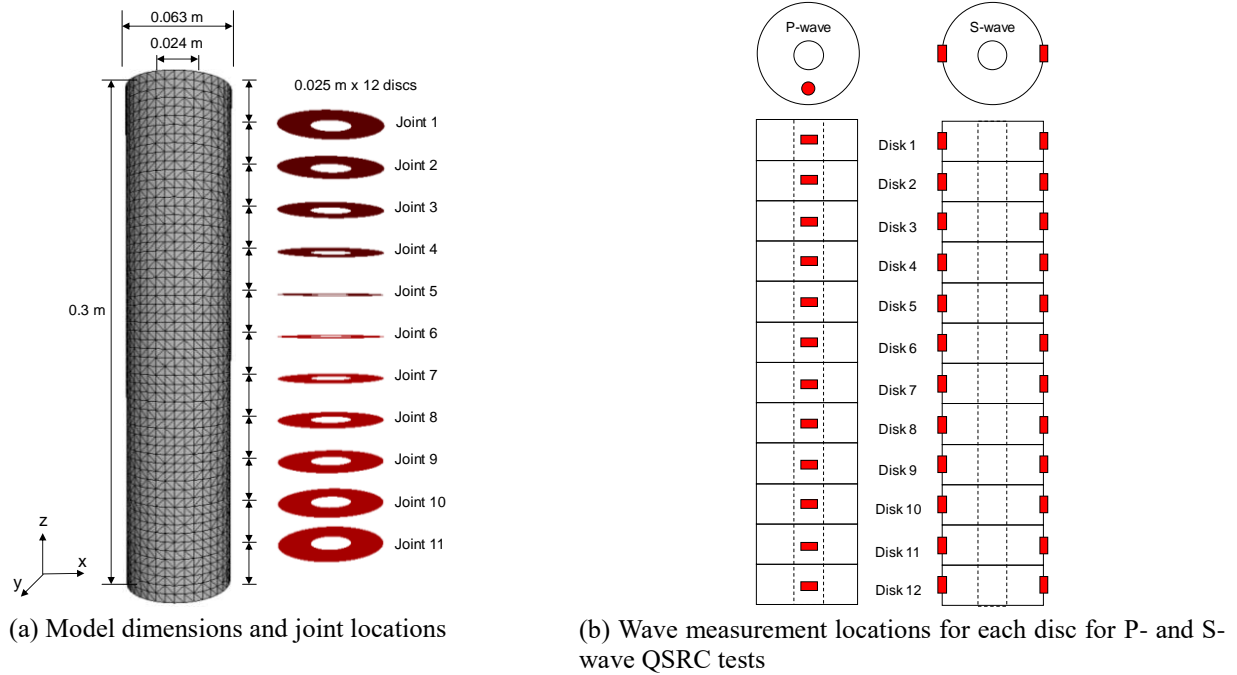


Fig. 5 3D model for jointed rock specimen

program (Itasca 2013). The discrete element method is widely used in rock engineering and rock mechanics owing to its ability to model the discrete discontinuous characteristics of rock masses. Fig. 5(a) shows the mesh and dimensions to simulate long-wavelength propagations in the repetitive disc-joint system.

To simulate the same joint condition as the experimental test, the joint surfaces in the numerical model were clean and flat, and all of the interface elements on one side of the disc were in full contact with all interface elements on the other side of the neighboring disc. A Coulomb-slip joint constitutive model was assigned to simulate the interfacing joints. Stress boundaries were assigned at the top of the specimen for both P- and S-wave simulations. The bottom boundary was fixed by setting the velocities in all directions to zero for S-wave simulations. Non-reflective viscous boundaries were assigned to the joints in the joint plane direction to minimize wave reflections at the joint interfaces. In addition to the measurement locations outlined in the experimental setup, additional measurement locations were added to each disc, as shown in Fig. 5(b), to better understand the P- and S-wave propagation characteristics throughout the repetitive rock-joint system.

### 3.2 Optimization of model parameters

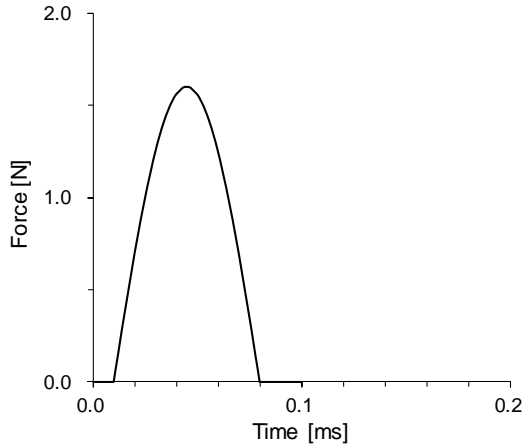
The 3DEC program uses an explicit time-marching scheme to calculate the equation of motion, which is expressed with finite differentiated displacement and stress terms for all grid points (Zhu *et al.* 2013). In each step, the velocities and stresses of all grid points are updated. However, it is assumed that the newly calculated stresses do not affect the present velocities of all grid points. Hence, the calculation is performed with known values that are obtained from the previous calculation process. This assumption can be justified using a small time step such that

the information cannot physically pass from one element to another in that interval (Howie and Amini 2005). In this concept, the calculated wave speed always remains ahead of the physical wave speed.

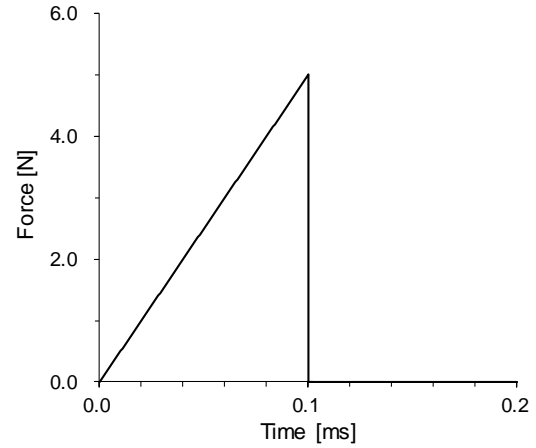
The maximum element size should be optimized to effectively simulate wave propagations using the discrete element method. Extremely large grid dimensions filter high frequencies, whereas extremely small grid dimensions cause numerical instabilities and require considerable computational cost (Villiappan and Murti 1984, Saenger *et al.* 2000). The grid size  $\Delta x$  is defined with the lowest velocity and highest frequency of the wave propagation (Zerwer *et al.* 2002):

$$\Delta x \leq \chi \cdot \lambda_{\min} \quad (4)$$

where  $\lambda_{\min}$  is the minimum wavelength of a propagating elastic wave ( $\lambda_{\min} = V_{\min}/f_{\max}$ ),  $V_{\min}$  the lowest elastic wave velocity of a medium,  $f_{\max}$  the highest frequency of a propagating wave, and  $\chi$  a constant ( $\chi = 0.25$  for consistent mass matrices;  $\chi = 0.2$  for lumped mass matrices). The Rayleigh wave velocity  $V_R$  in a homogeneous half-space is generally considered to be the lowest elastic wave velocity and is related to the S-wave velocity  $V_S$  by  $V_R \approx 0.9 V_S$  (Zerwer *et al.* 2002). In this study, the highest frequency range of a wave generated by an impact source was  $f_{\max} = 7,143$  Hz, and the Rayleigh wave velocity of the specimen varied from  $V_{\min} = 873$  m/s for acetal, which has the minimum wave velocity, to 2888 m/s for aluminum, which has the maximum wave velocity, resulting in a minimum wavelength of  $\lambda_{\min} = 0.122$  m. Because 3DEC uses lumped mass matrices as default, the allowable maximum dimension of the three-dimensional grid is 0.0244 m. In addition, the dimension of the grid should satisfy the Courant number  $\Delta x \leq \lambda_{\min}/6 = 0.02$  m (Robertsson *et al.* 1994). Hence, the finite grid size was determined to be  $\Delta x =$

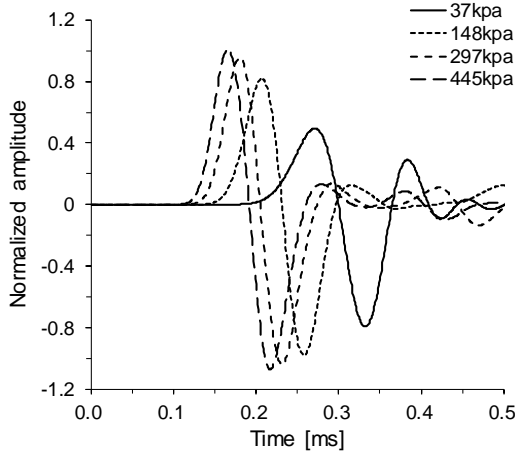


(a) Impulse excitation for longitudinal wave generation

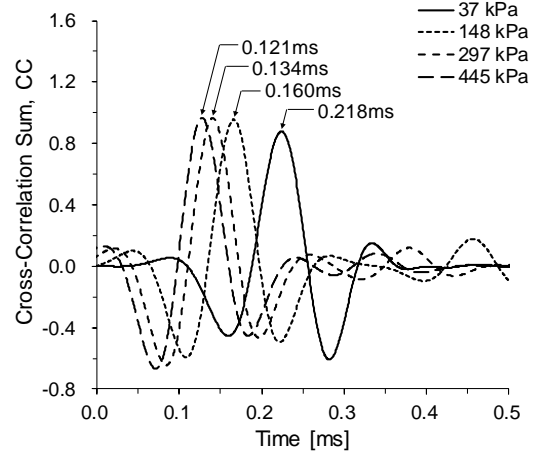


(b) Torsional excitation for shear wave generation

Fig. 6 Time-domain excitation signals applied to the upper end of rock column



(a) Received time-domain signals



(b) Cross-correlation sums and detected arrival times

Fig. 7 P-wave signals obtained from numerical analysis of the Gneiss specimen under different normal stress levels

0.005 m in this study.

The optimal range of the time increment can be calculated from the grid size  $\Delta x$  and the P-wave velocity  $V_p$  of the medium, in which wave propagation is expressed by the following equation (Villiappan and Murti 1984):

$$\frac{\Delta x}{10 \cdot V_p} \leq \Delta t \leq \frac{\Delta x}{V_p} \quad (5)$$

It is noteworthy that a larger time increment  $\Delta t$  yields a diverging solution, whereas a smaller time increment causes spurious oscillations (Gibbs phenomenon). In addition, the time increment should satisfy the temporal Nyquist limit:

$$\Delta t < \frac{1}{2 \cdot f_{\max}} \quad (6)$$

In this study, the time increment was calculated as  $\Delta t = 0.1 \mu\text{s}$ , which satisfies the spatial and temporal Nyquist limits simultaneously.

The time-domain excitation signals for the QSRC test are shown in Fig. 6. For the generation of P-waves in the vertical direction, a steel sphere of diameter 10 mm was

dropped freely onto the top of the rock column from a height of 0.2 m. The duration of the contact between the steel ball and the top of rock column can be calculated as follows (Sansalone and Carino 1986):

$$t_c = 5.97[\rho_s(\delta_s + \delta_m)]^{0.4} \frac{R}{H^{0.1}}, \quad (7)$$

where  $\delta_m = (1 - \nu_m^2)/E_m$ ,  $\delta_s = (1 - \nu_s^2)/E_s$ ,  $\rho_s$  the density of the steel sphere (7800 kg/m<sup>3</sup>),  $R$  the radius of the steel sphere (0.005 m),  $H$  the height of the free fall (0.2 m),  $\nu_m$  the Poisson ratio of the test material (0.2),  $\nu_s$  the Poisson ratio of the steel sphere (0.15),  $E_m$  the elastic modulus of the test material, and  $E_s$  the elastic modulus of the steel sphere (220 GPa). The maximum force and duration of impact were calculated as 1.6 N and 0.07 ms, respectively. For a longitudinal excitation, the calculated excitation signal was applied as a half sine function at the top of the rock column. For a torsional excitation, a force was applied linearly with time up to 5 N at 0.1 ms and then removed instantly. The excitation signal was applied at two locations on top of the specimen in opposite directions with respect to the central axis of the model to allow an accurate representation of free

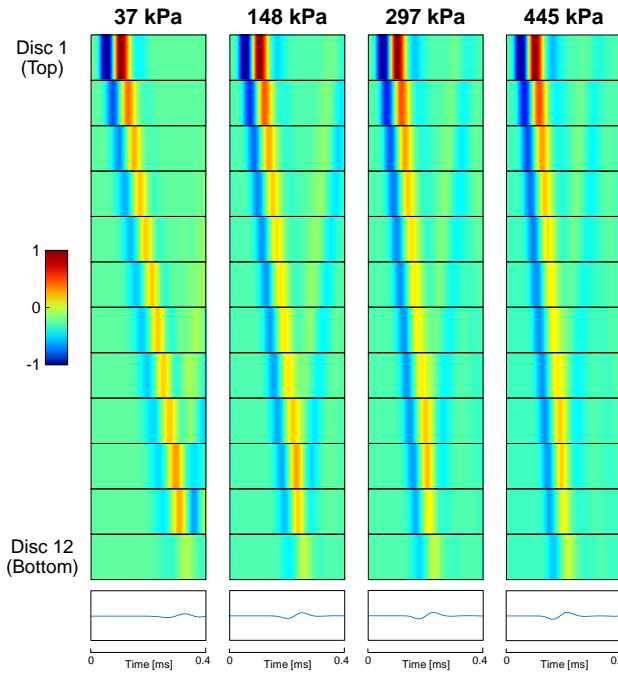
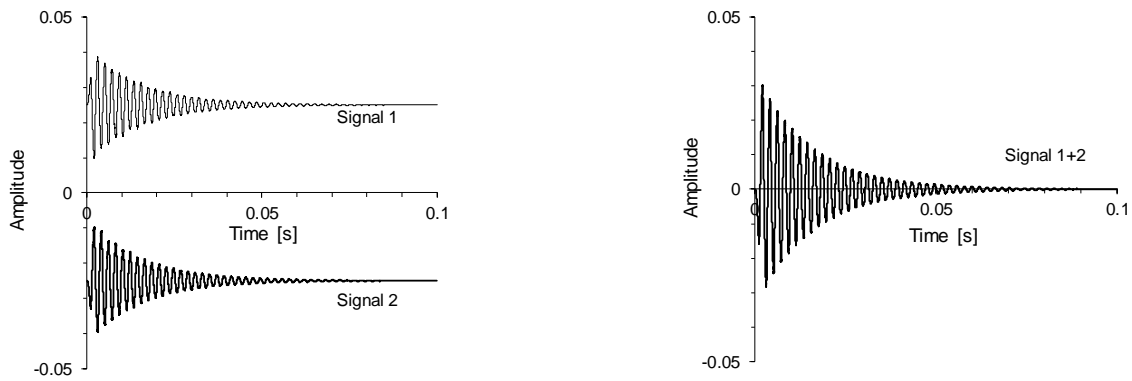
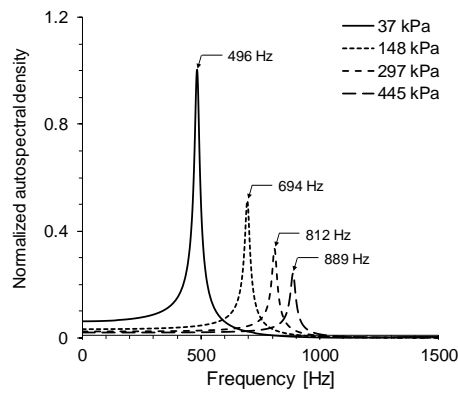


Fig. 8 Cascade of received P-wave signals in each rock disc for the gneiss specimen for different normal stress levels. The signal amplitude measured at each disc layer is illustrated in a color scale from 1 to -1, where red represents peaks and blue represents troughs. The time-domain data from the bottom disc is shown below the cascade for reference



(a) Time-domain signals obtained from two diametrically opposite measurement points

(b) Added time domain signal



(c) Frequency response transformed from the added time-domain signal for different normal stress levels

Fig. 9 S-wave signals obtained from numerical analysis

torsional vibrations. Both dynamic excitation inputs were applied as transient load boundaries to their respective

positions to provide a net torque to the sample. A Rayleigh mass-proportionate damping of 2% obtained from

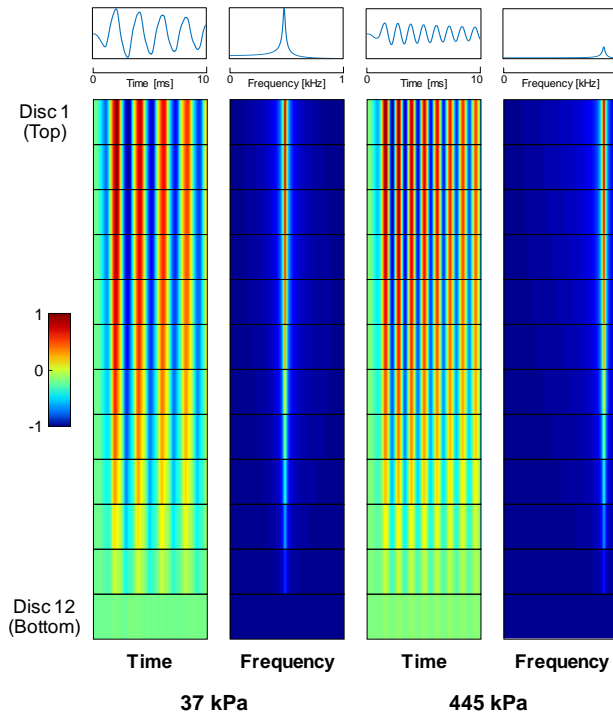


Fig. 10 Cascade of received S-wave time and frequency domain signals in each rock disc for the gneiss specimen for 37 and 445 kPa normal stresses. The signal amplitude measured at each disc layer is illustrated in a color scale from 1 to -1, where red represents peaks and blue represents troughs. The time- and frequency-domain data from the top disc is shown above the cascade for reference

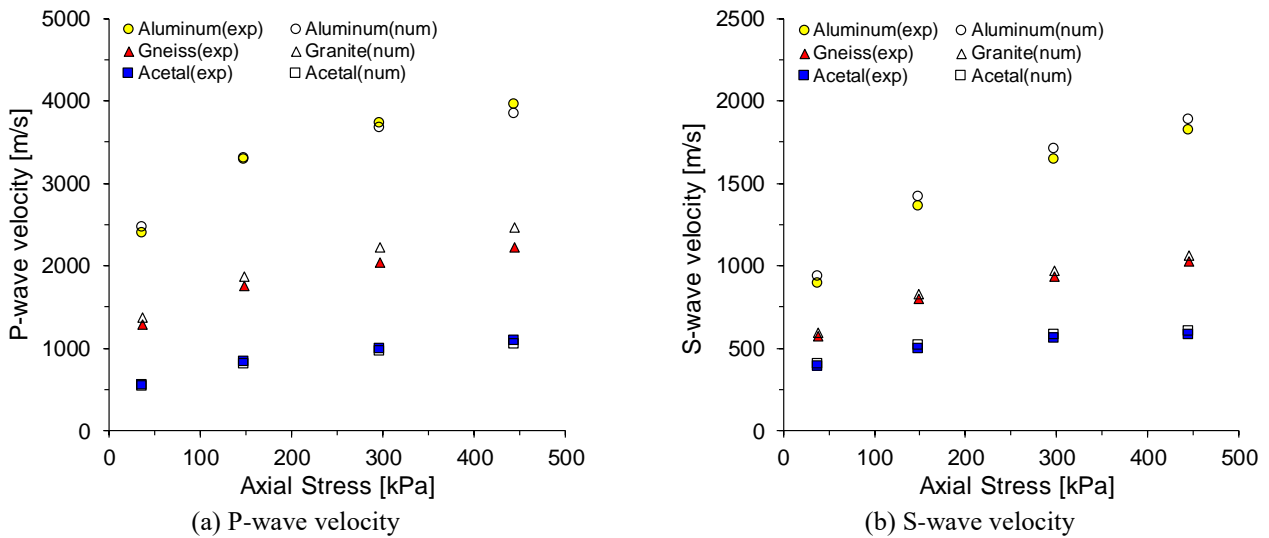


Fig. 11 Elastic wave velocities obtained from numerical analysis for different tested materials against normal stress levels. Wave velocities obtained from laboratory experiments are superimposed for each normal stress level and material, where (exp) denotes results from laboratory experiments and (num) denotes results from numerical analysis

experimental study was applied to simulate the mechanical damping in all cases. The damping ratio falls within the range of frequency-independent damping of geomaterials around 2-5% (Biggs 1964, Perino and Barla 2015).

### 3.3 Numerical results

Fig. 7(a) shows the P-wave arrival signals for different stress levels obtained at the bottom of the gneiss specimen.

The amplitudes of the received signals were normalized by the amplitude of the incident wave. The travel time can be calculated using the cross-correlation method considering the incident and received wave signals. Fig. 7(b) shows the cross-correlation sum of the P-wave according to the normal stress, where the time lag ahead of the peak of the cross-correlation sum represents the time difference. The numerical results show increased amplitudes and shorter time lags with increased normal stress, which implies that

higher energy is transmitted through the jointed rock mass with less attenuation for stiffer joint conditions. This is evident in the cascade of the received P-wave signals for different stress levels at each disc layer (Fig. 8). The color-scale and the received time-domain signal indicated improved energy transmission between joint interfaces with increased normal stress and joint stiffness. Clearly, the wave propagation in a repetitive jointed rock mass system is recognized by the travel time between discrete rock disc layers and across joint interfaces.

Figs. 9 (a) and 9(b) show the torsional shear signals and their added sum obtained at the top of the gneiss specimen. The frequency-domain signal transformed from the time-domain signals show a clear peak resonant frequency for all stress levels, as shown in Fig. 9(c). A higher applied stress level increased the resonant frequency and decreased the amplitude, implying changes in torsional vibration modes of the specimen with stiffer joint conditions. Unlike P-waves where the propagation direction is equal to the loading direction, the S-waves propagate perpendicular to the loading direction, and the increased normal stress hindered the torsional motion of the specimen with respect to the same applied torsional excitation. This was evident in the cascade of the received S-wave time domain signals for different stress levels at each disc layer (Fig. 10). The color scale and time-domain signal measured on top of the specimen indicated increased frequency and decreased amplitude with increased normal stress and joint stiffness. A clear shift in resonant frequency and decrease in amplitude were observed in the frequency cascade.

The P- and S-wave velocities for different materials obtained from the numerical simulation were compared with the experimental results (Fig. 11). The numerical P-wave velocities of acetal and aluminum agreed well with the experimental results, whereas the numerical P-wave velocities of the gneiss specimens were higher than the experimental results for all tested stress levels. This was primarily owing to the imperfectly smooth joint surfaces and minute asperities introduced in the sample preparation for the experimental tests. Artificial materials, such as acetal and aluminum, are homogeneous and enable an accurate fabrication of smooth joints with good precision. However, this idealized manufacturing of smooth surfaces is difficult to achieve for rocks that are innately heterogeneous. Rock disc cutting introduces minute asperities during the manufacturing process, which results in imperfect contact conditions between joints. Such apertures reduce the P-wave velocity in the disc-stacked column specimen. This was reflected in the errors between the P-wave velocity from the numerical and experimental results, where the average error was 3.7% and 1.9% for acetal and aluminum, respectively, and 8.5% for gneiss. Similarly, the torsional shear wave velocities from the numerical results agreed well with the experimental results for all specimens. The errors between the S-wave velocity results for all three materials indicated a consistent average between 3.7% and 4%, where the experimental values were always smaller than the numerical values for all tested normal stress levels.

#### 4. Conclusions

A preliminary numerical study on long-wavelength

elastic wave propagation in regularly jointed rock masses was presented herein. Experimental studies using the QSRC test device for regularly jointed disc column specimens were performed for three different materials (acetal, aluminum, and gneiss). The normal and shear joint stiffnesses were extracted from the experimental results using the equivalent continuum model and used as input parameters for numerical analysis. The jointed specimens were simulated using the 3DEC program, and numerical parameters were optimized for the time step, finite grid size, contact time, and force–time functions for effective numerical simulations. Using the calibrated jointed rock model, numerical analyses were performed, and the results were compared with the experimental results.

The long-wavelength P- and S-wave velocities of each specimen increased in both experimental and numerical studies with increased normal stress levels. The velocities obtained from the numerical analysis agreed well with the experimental results within allowable errors. The wave propagation and energy dissipation in jointed rocks were affected by the joint surface roughness. However, the ideal flat contact joint conditions simulated in the numerical model could not be fully achieved in the experimental tests because of minute apertures induced during sample preparation. These imperfections yielded smaller P- and S-wave velocities in the experimental results compared with the numerical results. Natural joint surfaces from the viewpoint of engineering applications are seldom clean nor ideally flat and are often rough with various degrees of asperities. This study provides a framework on which further parametric studies involving different joint conditions can be performed. Different field and joint conditions, such as stress anisotropy, water level, gouge fill, joint orientation, and joint spacing can be further simulated using the numerical model. However, the numerical simulation results should be adjusted accordingly based on the field joint conditions for practical purposes and applications, such as wave propagations in jointed rock masses induced by earthquakes or blasting.

#### Acknowledgments

This research was supported by the National Research Foundation of Korea (NRF) grant funded by the Korea Ministry of Science and ICT (MSIT) (No.2017R1A5A 1014883). The second author was supported by the Korea Ministry of Land, Infrastructure and Transport (MOLIT) as 「Innovative Talent Education Program for Smart City」.

#### References

- Brady, B.H. and Brown, E.T. (1993), *Rock Mechanics: For Underground Mining*, Springer Science & Business Media, Berlin, Germany.
- Biggs, J.M. (1964), *Introduction to Structural Dynamics*, McGraw-Hill, New York, U.S.A.
- Cai, J. and Zhao, J. (2000), "Effects of multiple parallel fractures on apparent attenuation of stress waves in rock masses", *Int. J.*

- Rock Mech. Min. Sci.*, **37**(4), 661-682.  
[https://doi.org/10.1016/S1365-1609\(00\)00013-7](https://doi.org/10.1016/S1365-1609(00)00013-7).
- Cha, M. and Cho, G.C. (2007), "Compression wave velocity of cylindrical rock specimens: Engineering modulus interpretation", *Jpn. J. Appl. Phys.*, **46**(7S), 4497.  
<https://doi.org/10.1143/JJAP.46.4497>.
- Cha, M., Cho, G.C. and Santamarina, J.C. (2009), "Long-wavelength P-wave and S-wave propagation in jointed rock masses", *Geophysics*, **74**(5), E205-E214.  
<https://doi.org/10.1190/1.3196240>.
- Chai, S., Li, J., Zhang, Q., Li, H. and Li, N. (2016), "Stress wave propagation across a rock mass with two non-parallel joints", *Rock Mech. Rock Eng.*, **49**(10), 4023-4032.  
<https://doi.org/10.1007/s00603-016-1068-z>.
- Cook, N.G. (1992). "Natural joints in rock: mechanical, hydraulic and seismic behaviour and properties under normal stress", *Int. J. Rock Mech. Min. Sci.*, **29**(3), 198-223.  
[https://doi.org/10.1016/0148-9062\(92\)93656-5](https://doi.org/10.1016/0148-9062(92)93656-5).
- Fratta, D. and Santamarina, J. (2002), "Shear wave propagation in jointed rock: State of stress", *Géotechnique*, **52**(7), 495-505.  
<https://doi.org/10.1680/geot.2002.52.7.495>.
- Goodman, R.E. (1989), *Introduction to Rock Mechanics*, Wiley, New York, U.S.A.
- Howie, J.A. and Amini, A. (2005), "Numerical simulation of seismic cone signals", *Can. Geotech. J.*, **42**(2), 574-586.  
<https://doi.org/10.1139/t04-120>.
- Itasca, C. (2013), *3DEC, Software, Version 5.0*, Minneapolis, Minnesota, U.S.A.
- Ju, Y., Sudak, L. and Xie, H. (2007), "Study on stress wave propagation in fractured rocks with fractal joint surfaces", *Int. J. Solids Struct.*, **44**(13), 4256-4271.  
<https://doi.org/10.1016/j.ijsolstr.2006.11.015>.
- Kim, J.W., Chong, S.H. and Cho, G.C. (2018), "Experimental characterization of stress-and strain-dependent stiffness in grouted rock masses", *Materials*, **11**(4), 524.  
<https://doi.org/10.3390/ma11040524>.
- Li, H., Liu, T., Liu, Y., Li, J., Xia, X. and Liu, B. (2016), "Numerical modeling of wave transmission across rock masses with nonlinear joints", *Rock Mech. Rock Eng.*, **49**(3), 1115-1121. <https://doi.org/10.1007/s00603-015-0766-2>.
- Li, J., Li, H., Jiao, Y., Liu, Y., Xia, X. and Yu, C. (2014), "Analysis for oblique wave propagation across filled joints based on thin-layer interface model", *J. Appl. Geophys.*, **102**, 39-46.  
<https://doi.org/10.1016/j.jappgeo.2013.11.014>
- Li, J., Ma, G. and Zhao, J. (2010), "An equivalent viscoelastic model for rock mass with parallel joints", *J. Geophys. Res. Solid Earth*, **115**(B3). <https://doi.org/10.1029/2008JB006241>.
- Li, J.C., Wu, W., Li, H., Zhu, J. and Zhao, J. (2013), "A thin-layer interface model for wave propagation through filled rock joints", *J. Appl. Geophys.*, **91** 31-38.  
<https://doi.org/10.1016/j.jappgeo.2013.02.003>.
- Mindlin, R.D. (1960), *Waves and Vibrations in Isotropic, Elastic Plates*, in *Structural Mechanics*. Pergamon Press, New York, U.S.A., 199-232.
- Mohd-Nordin, M.M., Song, K.I., Cho, G.C. and Mohamed, Z. (2014), "Long-wavelength elastic wave propagation across naturally fractured rock masses", *Rock Mech. Rock Eng.*, **47**(2), 561-573. <https://doi.org/10.1007/s00603-013-0448-x>.
- Perino, A., Zhu, J., Li, J., Barla, G. and Zhao, J. (2010), "Theoretical methods for wave propagation across jointed rock masses", *Rock Mech. Rock Eng.*, **43**(6), 799-809.  
<https://doi.org/10.1007/s00603-010-0114-5>.
- Perino, A. and Barla, G. (2015), "Resonant column apparatus tests on intact and jointed rock specimens with numerical modelling validation", *Rock Mech. Rock Eng.*, **48**(1), 197-211.  
<https://doi.org/10.1007/s00603-014-0564-2>.
- Pyrak-Nolte, L.J., Myer, L.R. and Cook, N.G. (1990), "Transmission of seismic waves across single natural fractures", *J. Geophys. Res. Solid Earth*, **95**(B6), 8617-8638.  
<https://doi.org/10.1029/JB095iB06p08617>.
- Robertsson, J.O., Blanch, J.O. and Symes, W.W. (1994), "Viscoelastic finite-difference modeling", *Geophysics*, **59**(9), 1444-1456. <https://doi.org/10.1190/1.1443701>.
- Saenger, E.H., Gold, N. and Shapiro, S.A. (2000), "Modeling the propagation of elastic waves using a modified finite-difference grid", *Wave Motion*, **31**(1), 77-92.  
[https://doi.org/10.1016/S0165-2125\(99\)00023-2](https://doi.org/10.1016/S0165-2125(99)00023-2).
- Sansalone, M. and Carino, N.J. (1986), "Impact-echo: A method for flaw detection in concrete using transient stress waves", NBSIR 86-3452, US Department of Commerce, National Bureau of Standards, National Engineering Laboratory, Center for Building Technology, Structures Division, U.S.A.
- Schoenberg, M. (1980), "Elastic wave behavior across linear slip interfaces", *J. Acoust. Soc. Am.*, **68**(5), 1516-1521.  
<https://doi.org/10.1121/1.385077>.
- Schoenberg, M. and Muir, F. (1989), "A calculus for finely layered anisotropic media", *Geophysics*, **54**(5), 581-589.  
<https://doi.org/10.1190/1.1442685>.
- Schoenberg, M. and Sayers, C.M. (1995), "Seismic anisotropy of fractured rock", *Geophysics*, **60**(1), 204-211.  
<https://doi.org/10.1190/1.1443748>.
- Tao, M., Chen, Z., Li, X., Zhao, H. and Yin, T. (2016), "Theoretical and numerical analysis of the influence of initial stress gradient on wave propagations", *Geomech. Eng.*, **10**(3), 285-296. <https://doi.org/10.12989/gae.2016.10.3.285>.
- Villiappan, S. and Murti, V. (1984), "Finite element constraints in the analysis of wave propagation problem", UNICV Report No.48, R-218, School of Civil Engineering, University of New South Wales, Australia.
- Wang, R., Hu, Z., Zhang, D. and Wang, Q. (2017), "Propagation of the stress wave through the filled joint with linear viscoelastic deformation behavior using time-domain recursive method", *Rock Mech. Rock Eng.*, **50**(12), 3197-3207.  
<https://doi.org/10.1007/s00603-017-1301-4>.
- White, J.E. (1983), *Underground Sound: Application of Seismic Waves*, Elsevier Science Publishing Company Inc, Amsterdam, The Netherlands.
- Wu, N., Liang, Z., Li, Y., Qian, X. and Gong, B. (2019), "Effect of confining stress on representative elementary volume of jointed rock masses", *Geomech. Eng.*, **18**(6), 627-638.  
<https://doi.org/10.12989/gae.2019.18.6.627>.
- Zerwer, A., Cascante, G. and Hutchinson, J. (2002), "Parameter estimation in finite element simulations of Rayleigh waves", *J. Geotech. Geoenviron. Eng.*, **128**(3), 250-261.  
[https://doi.org/10.1061/\(ASCE\)1090-0241\(2002\)128:3\(250\)](https://doi.org/10.1061/(ASCE)1090-0241(2002)128:3(250)).
- Zhao, X., Zhao, J., Cai, J. and Hefny, A.M. (2008), "UDEC modelling on wave propagation across fractured rock masses", *Comput. Geotech.*, **35**(1), 97-104.  
<https://doi.org/10.1016/j.compgeo.2007.01.001>
- Zhu, J., Deng, X., Zhao, X. and Zhao, J. (2013), "A numerical study on wave transmission across multiple intersecting joint sets in rock masses with UDEC", *Rock Mech. Rock Eng.*, **46**(6), 1429-1442. <https://doi.org/10.1007/s00603-012-0352-9>.
- Zhu, J., Zhao, X., Wu, W. and Zhao, J. (2012), "Wave propagation across rock joints filled with viscoelastic medium using modified recursive method", *J. Appl. Geophys.*, **86**, 82-87.  
<https://doi.org/10.1016/j.jappgeo.2012.07.012>.